A detailed mechanism of degradation behaviour of biodegradable as-ECAPed Zn-0.8Mg-0.2Sr with emphasis on localized corrosion attack

Jan Pinc [a,*], Andrea Školáková [a], Vojtěch Hybášek [b], Šárka Msallamová [b], Petr Veřtát [a], Petr Ashcheulov [a], Martin Vondráček [a], Jan Duchoň [a], Ingrid McCarroll [c], Matěj Hývl [a], Swarnendu Banerjee [a], Jan Drahokoupil [a], Jiří Kubásek [b], Dalibor Vojtěch [b], Jaroslav Čapek [a]

[a] Institute of Physics of the Czech Academy of Sciences, Na Slovance 1999/2, Prague 8, 182 21, Czech Republic
[b] University of Chemistry and Technology, Faculty of Chemical Technology, Department of Metals and Corrosion Engineering, Technická 5, 166 28, Praha 6 – Dejvice, Czech Republic
[c] Max-Planck-Institut Für Eisenforschung, Max-Planck-Straße 1, 40237, Düsseldorf, Germany

ARTICLE INFO

ABSTRACT

In this study, advanced techniques such as atom probe tomography, atomic force microscopy, X-ray photoelectron spectroscopy, and electrochemical impedance spectroscopy were used to determine the corrosion mechanism of the as-ECAPed Zn-0.8Mg-0.2Sr alloy. The influence of microstructural and surface features on the corrosion mechanism was investigated. Despite its significance, the surface composition before exposure is often neglected by the scientific community. The analyses revealed the formation of thin ZnO, MgO, and MgCO$_3$ layers on the surface of the material before exposure. These layers participated in the formation of corrosion products, leading to the predominant occurrence of hydrozincite. In addition, the layers possessed different resistance to the environment, resulting in localized corrosion attacks. The segregation of Mg on the Zn grain boundaries with lower potential compared with the Zn-matrix was revealed by atom probe tomography and atomic force microscopy. The degradation process was initiated by the activity of micro-galvanic cells, specifically Zn – Mg$_2$Zn$_{11}$/SrZn$_{13}$. This process led to the activity of the crevice corrosion mechanism and subsequent attack to a depth of 250 μm. The corrosion rate of the alloy determined by the weight loss method was 0.36 mm·a^{-1}. Based on this detailed study, the degradation mechanism of the Zn-0.8Mg-0.2Sr alloy is proposed.

1. Introduction

Biodegradable materials are a group of materials designed to gradually degrade *in vivo,* without any adverse effects on the host organism [1]. The degradation rate of these materials should be comparable with the speed of new tissue growth [2], ensuring the compactness of the regenerated tissue in the implanted area without the presence of cavities. Furthermore, the mechanical properties should be appropriate for the intended use and remain stable for a relatively long period of time (2–6 months) as the newly formed tissue gradually takes over the mechanical load [3–5]. Based on these requirements, metallic materials were identified as promising materials for load-bearing applications [6]. The group of metallic biodegradable materials predominantly consists of iron, magnesium, and zinc [7]. Among all of the mentioned materials, zinc excels in its degradation behaviour possessing an almost ideal

corrosion rate and absence of hydrogen gas evolution during corrosion [8], indicating its significant potential for the fabrication of biodegradable implants.

Zinc is an essential element for various functions in the human body [9]. One of the most important functions of zinc is its participation in the growth of bone [10,11], suggesting a positive influence of zinc implants during bone healing. However, the effect is strongly dependent on zinc concentration in the area near the implanted material. On one hand, zinc deficiency leads to serious complications and illnesses (skeletal and brain evolution, atherosclerosis, autonomic disorders, etc.) [12]. On the other hand, the excess of zinc leads to a decrease in copper concentrations and subsequently to the disorder of haematogenesis [13]. For these reasons, it is necessary to reliably determine *in vitro* corrosion behaviour to reduce the risk of negative reactions in the body. Despite the relatively high number of publications concerning the corrosion behaviour

---

of zinc and its alloys, there are still gaps within the literature that need to be elucidated. Examples of such gaps are connected, especially, with the standardisation of the *in vitro* environments (the best agreement with *in vivo* results) [14], the influence of the individual phases and their distribution [15,16], the influence of the processing methods on the corrosion behaviour [17] and the influence of native surface layers on corrosion attack.

The drawbacks regarding the strength and low ductility of as-cast, zinc-based materials are well known [18–20]. However, many approaches leading to an improvement in mechanical properties have been successfully applied and have contributed to the usability of these materials in the field of biodegradable implants [21–24]. Generally, the addition of alloying elements is often used to achieve this purpose. The selection of the alloying elements is restricted by several criteria, including non-toxicity and modifying mechanical behaviour to fulfil the requirements of medical applications [25]. For this reason, elements such as magnesium [26], calcium [22], strontium [27], lithium [28], manganese [29], and silver [30] are often used for alloying of pure zinc. Moreover, the Zn-based alloys are further processed by suitable thermomechanical treatment, leading to a significant improvement of their mechanical performance via grain refinement and surface texture modification as in the case of rolling [31], extrusion [32], high-pressure torsion (HPT) [33], or equal channel angular pressing (ECAP) [34]. The ECAP process, especially the Bc route, leads to significant improvements in the mechanical properties of Zn-based alloys, such as strength and ductility, by homogenizing the microstructure and refining the grain size [35]. Additionally, the process leads to minimal anisotropy of mechanical properties in different directions [34], which can be beneficial for implants loaded in more than one direction, for example plates and scaffolds.

The Zn-XMg (X = 1 wt %) and Zn–Mg–Sr alloys have been studied for medical applications due to their ability to degrade in the body and eliminate the need for retrieval surgery [24,26,36,37]. However, the corrosion behaviour of these alloys in simulated body fluid (SBF) is not fully understood. Available studies have reported inconsistent results, with some showing improved corrosion resistance while others have shown increased corrosion rates of the same materials. To perform relevant comparison of the results obtained in this study and by other scientific teams, only works where the experiments were performed at comparable conditions (i.e. Zn–Mg alloys exposed for 7–21 days in SBF at 37 °C) are referred. Vojtěch et al. found minimal changes in corrosion rate of as-cast Zn-XMg (X = 1 wt %) systems exposed to simulated body fluid [38]. This was attributed to the negligible participation of micro-galvanic cells in the corrosion process. However, other studies have found significant influence of micro-galvanic cells on the corrosion process of the same system [39,40]. Similar inconsistencies can also be observed in the case of the formation of different corrosion products (complex Zn compounds, PO_4^{3-} based compounds) [40–43]. The differences in results between the individual studies may also be attributed to variations in the experimental conditions (such as composition [44] and temperature of the SBF [45,46]) or neglecting the initial state of the material surface before exposure. In addition to the inconsistency of the published information, the characterization of the surface composition prior to exposure is often missing. However, the surface composition appears to be crucial for subsequent degradation and for a thorough understanding of the process. This lack of consistent data and missing information highlights the need for a more comprehensive study that will provide a detailed understanding of the corrosion process of these alloys in SBF with all measurements done under the same conditions.

In this study, the corrosion behaviour of a Zn-0.8Mg-0.2Sr (wt. %) alloy processed by ECAP was characterized using immersion and electrochemical measurements. A strong emphasis was placed on the influence of grain size, distribution of the secondary phases and presence of native surface layers on the corrosion process. Such a comprehensive approach has not been used for the investigation of corrosion of Zn-based biodegradable materials, to the best of our knowledge.

Therefore, the obtained results allow us to propose the corrosion mechanism of the investigated Zn-based alloy and extend current knowledge regarding the corrosion of Zn-based biodegradable materials.

2. Experiment

Pure zinc, magnesium, and strontium in a weight ratio (99:0.8:0.2) were melted in the electric resistance furnace at 520 °C without the use of a protective atmosphere. The ratio between the alloying elements was chosen to obtain an ideal balance between mechanical (Table 1) and corrosion characteristics, and to be able to compare all results within our studies performed on the Zn–Mg–Sr alloys reliably.

The melted mixture of the metals was mixed using a graphite rod in order to homogenize the composition; subsequently, the melt was cast into a steel mould with a 50 mm diameter. During the casting process, the mixture was filtered using an Al_2O_3 frit with average pore size of 3 mm to remove the oxides from the melt. The cooled ingot was annealed for 24 h at 350 °C to homogenize the phase composition of the material. After the annealing, the ingot was quenched into the water and used for further processing. Blocks with a side length of 10 mm and a height of 70 mm were cut from the centre of the ingot using a CNC electroerosive machine Agiecharmilles FI240 (EEC). The samples prepared in this way were lubricated using a high-temperature paste GLEIT-μ HP 505 and processed by ECAP method. The angle of the die channel was Φ = 90°, and the pressing speed was set to 0.2 mm s^{-1}. Bc route (rotation by 90°) was used with first two passes performed at 200 °C and the following two passes at 150 °C. The temperatures were chosen to obtain the highest possible Zener-Hollomon parameter without damaging the sample. Subsequently, the samples were characterized using an FEI 3D Quanta 3D field-emission-gun DualBeam scanning electron microscope (SEM) equipped with Focused Ion Beam (FIB) lift-out technique and an FEI Tecnai G2 F20 X-TWIN transmission microscope (TEM). TEM measurements were performed at 200 kV. Phase composition of the alloy was determined using X-ray diffraction, and the detailed description of the analyses and their evaluation can be found in our previous study [34]. Samples were prepared for atom probe tomography (APT) using a Dual Beam Ga-FIB FEI Helios 600 using the lift-out protocol described by Thompson et al., 2007 [47]. A final accelerating voltage of 5 kV and a milling current of 47 pA were used to limit the damage caused by the Ga ions. Atom probe tips were then run on a LEAP5000 XR using voltage pulsing with a 15% pulse fraction, 200 kHz pulse frequency, and a 1% detection rate. Reconstruction of the data was undertaken using AP Suite 6.1. X-ray photoemission spectroscopy (XPS) core level spectra were measured at NanoESCA (Omicron) in normal emission configuration using monochromatized Al K$_\alpha$ radiation (hν = 1486.7 eV). The spectra were measured on the surface of the Zn-0.8Mg-0.2Sr sample and almost pure Mg_2Zn_{11} phase (95 wt % Mg_2Zn_{11}; 5 wt % Zn) three days after the sample polishing. The Mg_2Zn_{11} phase was prepared using pure metals (Zn and Mg) and melted under an argon atmosphere using an induction furnace. Subsequently, the phase was annealed at 350 °C for 24 h to homogenize the phase composition. The Mg_2Zn_{11} phase was analysed due to the determination of the influence of the intermetallic phases on the surface composition. Kelvin Probe Force Microscopy analyses (KPFM) were performed using a Bruker Dimension Icon atomic force microscope (AFM). Before the measurements, polished samples (Eposil F suspension) were rinsed by water, ethanol, and ultrasonically cleaned in

Table 1
Mechanical properties of the as-ECAPed Zn-0.8Mg-0.2Sr alloy.

Direction[a]	CYS (MPa)	UCS (MPa)	TYS (MPa)	UTS (MPa)	Ductility (%)	Reference
ED	252 ± 4	276 ± 7	207 ± 5	298 ± 4	12.2 ± 1.3	[34]

[a] Please see the designation of the sample directions in Fig. 1.

order to remove the residues after polishing. AFM was used to obtain sample topography and surface potential difference signal using amplitude-modulated two-pass method (AM – KPFM) [48]. For all the measurements, doped-diamond coated DDESP-FM-V2 probe was used with a tip radius of 100–120 nm, tip back and front angles of 17.5 ± 2.5 and $25 \pm 2.5°$, respectively, and Sb–Si cantilever with Al back-side coating. For the measurements, the sample (ED direction, Fig. 1) was divided into 4 quadrants with one measurement (simultaneous topography and potential measurement) performed in each individual quadrant. In each sector, 80×80 μm maps were acquired. Besides, one map with 150×150 μm size was acquired in the first quadrant, as well. The depth and potential line profiles were processed using Gwyddion software [49].

The corrosion behaviour of the ECAPed samples was evaluated using electrochemical and immersion tests. Electrochemical corrosion measurements were performed on degreased samples (Fig. 1a, ground on FEPA P2500) in a polymethylpentene cell with an electrolyte volume of 80 ml. The corrosive medium consisted of a solution of aerated simulated body fluid (SBF27 [44]). The temperature was set at 37 °C. A three-electrode setup was used, a silver-chloride electrode (SSCE; 3 mol kg^{-1} KCl, +0.21 V/SHE) and vitreous carbon rod were used as the reference and counter electrodes, respectively. The first two measurements consisted of 12 h of stabilization supplemented by measurements of open circuit potential (E$_{OC}$) and polarization resistance in the range of ± 20 mV/E$_{OCP}$ with a scan rate of 0.125 mV s^{-1}. The measurement sequence was closed by either anodic potentiodynamic polarization measured from -0.05 V/E$_{OC}$ to 1 V/E$_{OC}$, or cathodic polarization from 0.05 V/E$_{OC}$ to -1 V/E$_{OC}$, in both cases, the scan rate was 1 mV s^{-1}. The second electrochemical experiment consisted of cyclic measurements (3 times per hour) of impedance spectra in the range 10 kHz to 1 Hz, supplemented by spectra measured once every 7 h in the range 50 kHz–100 mHz with a total exposure time of 72 h. DC component corresponds to E$_{OC}$ and an AC potential to 10 mV. Seven points per decade were measured. This measurement was also complemented by an E$_{OC}$ measurement. The Gamry Reference 600 potentiostat was used to perform the measurements. The validity of the second type of impedance data was verified using the Kramers-Kronig transformation (obtained deviations are in the order of $2 \bullet 10^{-5}$ and lower) using Gamry Echem Analyst software. The Zview software was used for data fitting.

The samples used for the immersion tests (Fig. 1b) were ground up to P2500 SiC sandpapers and subsequently rinsed by ethanol and acetone. These samples were exposed in SBF for 72 h and 14 days at 37 °C. The ratio between the sample surface and the volume of the SBF was 80 ml cm^{-2} for all exposed samples, and the exposure took place under an air atmosphere. Besides that, the pH values were measured regularly, every second day of the exposure. The immersion tests started 3 days after the polishing in order to interconnect the results with these obtained by XPS measurements. In the case of the sample exposed for 72 h, the sample was attached into a polymer tube filled with the SBF solution. The sample was analysed in this experimental setup using Zeiss Xradia 610 Versa (μCT) under following conditions: voxel size 1.35 μm, 140 kV,

HE2 filter, a source distance of 13.55 mm, and a detector distance of 55 mm. The results obtained by μCT measurement were processed using Dragonfly software v.2022.1. After the 72 and 24 h exposures, the samples were removed from solution, rinsed by ethanol, and dried in air. Corrosion products formed on the material surface after 72 h were analysed using SEM-EDS. In addition, the products formed after 14 days of exposure were observed and analysed using optical microscope Olympus SZX9 (LM), SEM-EDS, TEM, X-ray diffraction (XRD) and Raman spectroscopy. The scraped corrosion products were crushed in the agate bowl and applied in ethanol to the copper mesh. TEM and STEM was performed at 200 kV and the diffraction patterns were processed using CrysTBox software [50]. XRD measurements were performed using a PANalytical X`Pert PRO powder diffractometer with a Co anode (K$_{\lambda 1}$ = 0.1789 nm, K$_{\lambda 2}$ = 0.1793 nm) in Bragg-Brentano geometry. PDF-4+ structure database [51] was used for phase identification and DIFFRAC.TOPAS for the Rietveld refinement. Raman measurements were performed at ambient temperature using a Renishaw InVia Raman Microscope under the following conditions: laser excitation wavelength of 488 nm with a laser power at the sample of 6 mW, × 50 Olympus objective, 65 μm slit, spot focus and the grating of 2400 lines/mm. Subsequently, the corrosion products were chemically removed using a solution containing chromium oxide and natrium sulphate according to the ASTM E407 standard, and the corrosion rate was calculated from the weight losses (ASTM G31-72 standard). The solutions were analysed every second day of exposure in two different ways. Firstly, 20 ml of the solution was removed from the top part of the container without mixing of the solution to measure the ion content of individual elements in the medium (labelled as a medium without sediments). Secondly, the rest of the solution was acidified using 1 ml of nitric acid in order to dissolve the precipitates and to determine the content of individual ions bonded in the corrosion products (labelled as medium with dissolved sediments). These solutions were analysed using an atomic absorption spectrometer Agilent 280FS AA (AAS).

3. Results

3.1. Microstructure

Microstructure of the as-ECAPed Zn-0.8Mg-0.2Sr alloy was extensively studied in our previous study [34]. Thus, the composition, distribution of the intermetallic phases, and grain size will be discussed in brief, due to the correlation between microstructure and corrosion behaviour. ECAPed material consisted of three different phases homogeneously distributed in the material structure; namely, Zn-based solid solution matrix, Mg$_2$Zn$_{11}$, and SrZn$_{13}$ phases. The SrZn$_{13}$ phase was localized predominantly within Mg$_2$Zn$_{11}$ intermetallic regions, which were surrounded by the zinc grains (Fig. 2a), these phases were also confirmed by XRD analyses. Most of the zinc grains were recrystallized with average size of 2.5 ± 1.4 μm; however, a small portion of non-recrystallized grains with a size of up to 40 μm was observed as well. The situation was slightly different in the intermetallic regions (Fig. 2b),
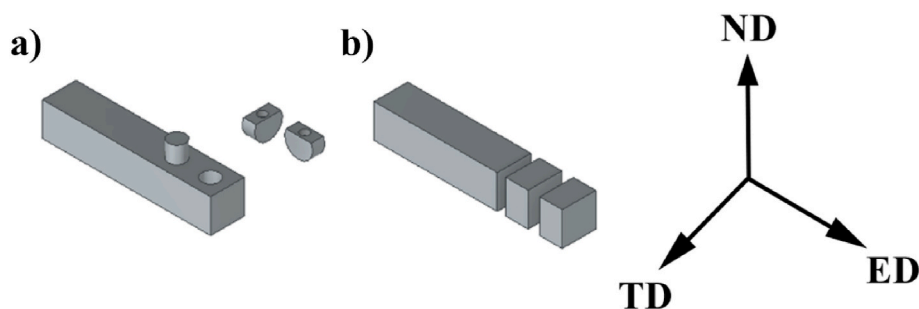

Fig. 1. Dimensions and locations of the samples used for the a) electrochemical and b) immersion measurements with labelling of individual directions (ED = extrusion direction, ND = normal direction, TD = transverse direction).
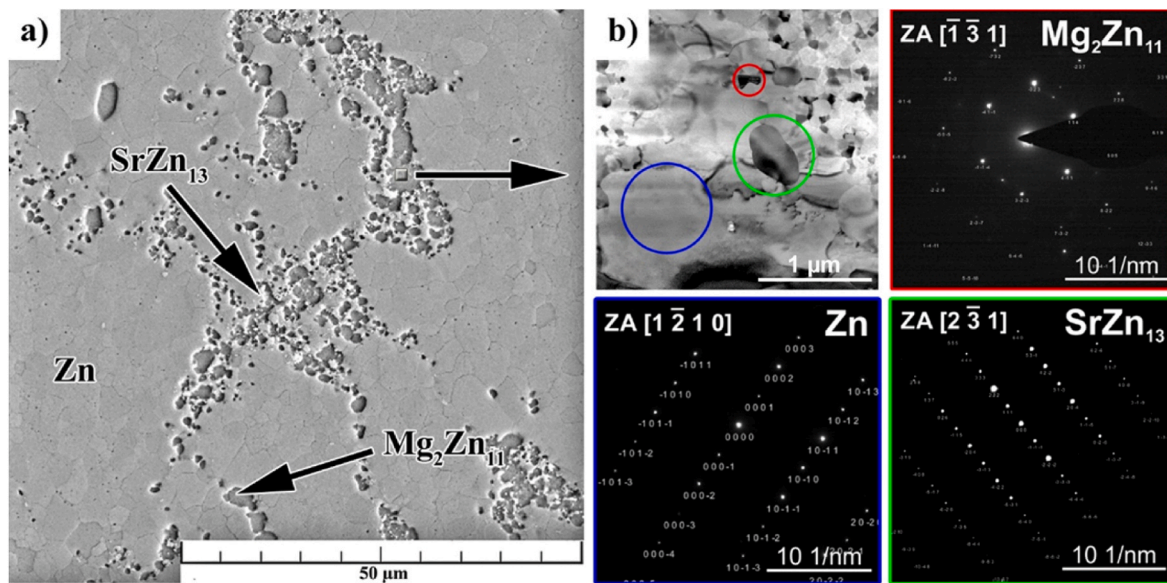
Fig. 2. a) SEM image of ECAPed Zn-0.8Mg-0.2Sr alloy microstructure with b) microstructural and phase composition of the intermetallic regions determined by TEM and SAED (circles represent individual phases – Zn (blue), Mg_2Zn_{11} (red) and $SrZn_{13}$ (green)).

where zinc grains with a size of 113 ± 57 nm were observed. Particles of the strontium-based phase were approximately 200 nm in size and were spherical in shape. Presence of larger particles of Mg_2Zn_{11} phase was observed in the intermetallic regions (approximately 500 nm), however, only a limited number of these large Mg_2Zn_{11} particles were present. For more detailed microstructural characterization, please see our previous
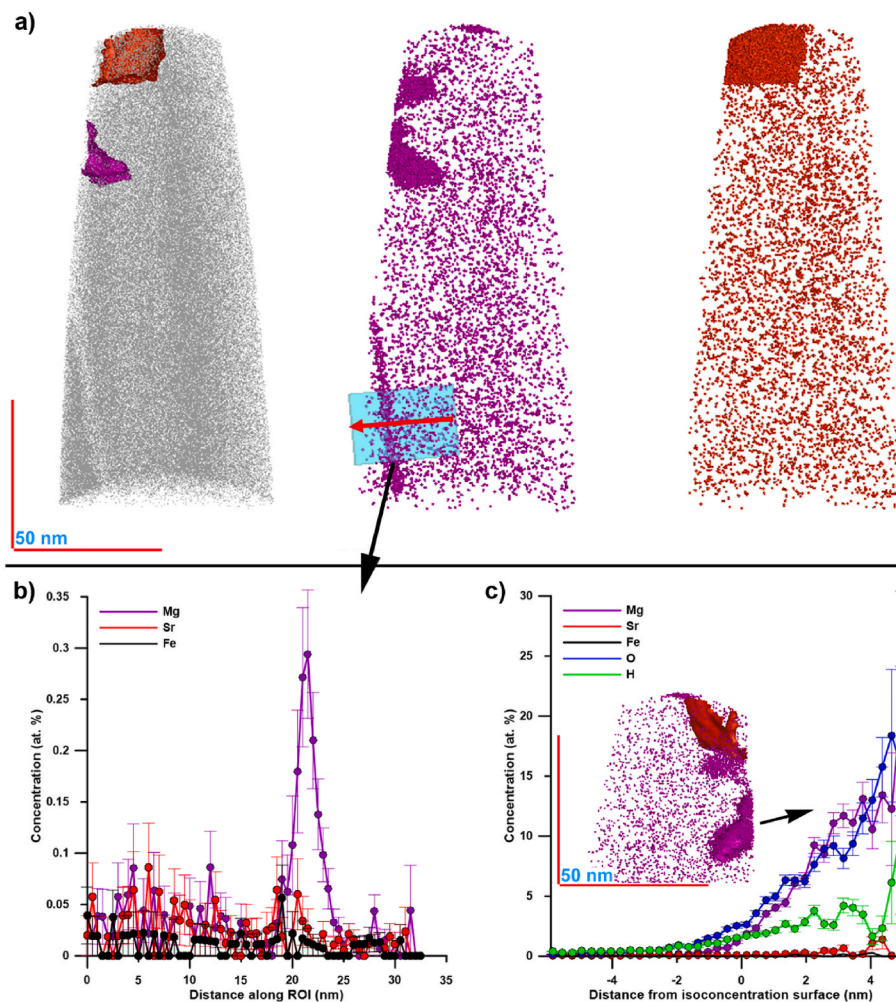

Fig. 3. a) Three atom probe maps showing first 1% of all Zn ions, second Mg ions and third Sr ions. The isoconcentration surfaces shown in the Zn ion map indicate a 4.65 at.% Sr surface (orange), and a 1.65 at.% Mg surface (purple). b) A 1D concentration profile through the region indicated in the Mg ion map, indicates segregation of Mg to the Zn grain boundary. c) A proximity histogram calculated from the Mg isoconcentration surface, providing chemical composition of the precipitate, note that Zn represents the remainder of atoms in the precipitate.

publication [34].

In addition, APT was used to characterize the local element distribution within the Zn-based alloy, the results obtained by APT are summarized in Fig. 3. The near atomic resolution of APT provides information regarding element segregation at grain boundaries and precipitate interfaces, as well as detailed compositional analysis of nanoscale precipitates, thereby aiding assessment of the influence of chemical composition on the alloy's corrosion behaviour. To ascertain the amounts of alloying elements in solution in the zinc matrix, an area distinct from the precipitates and grain boundary was extracted, in this case the mid-lower right section of the data, and a bulk concentration analysis was determined, Table 2. The results in Table 2 indicate that the zinc matrix contains only negligible amounts of dissolved magnesium, while low but non-negligible amounts of strontium were found in solid solution. A small amount of iron was also detected in the zinc matrix. Iron can be considered an impurity in the investigated alloy.

In the Zn-based matrix we also observed Sr and Mg containing precipitates. In the case of the Mg-based intermetallic phases, presence of oxygen in an Mg:O ratio of 1:1 was observed, suggesting the presence of oxidized Zn–Mg precipitates (Fig. 3c). Sr-based intermetallic phases were identified with a Zn:Sr ratio of 9:1, which is slightly different to the observations from previous diffraction measurements [34]. This chemical composition is still close to the $SrZn_{13}$ and the deviation of the exact stoichiometric composition could result from a loss of zinc signal in the atom probe data, possibly caused by a large number of multiple hit events. Alternatively, it could result from partial substitution of Sr by Zn in the precipitates. The observation of hydrogen at the precipitate is assumed to be caused by an evaporation field difference between the precipitate and the matrix and therefore represents hydrogen resulting from the experimental process and not a hydroxide. One of the most important findings was connected with the segregation of magnesium to the zinc grain boundaries (Fig. 3b). Concentration of the magnesium at the observed grain boundary was approximately 0.3 at. % without the presence of other metals (Fe, Sr) or oxygen. This suggests that in the investigated alloy, only Mg segregates to the grain boundaries.

The surface of the studied material and as-cast Mg_2Zn_{11} phase were also examined using X-ray photoelectron spectroscopy in order to describe the initial state of the material surface before corrosion testing. According to the composition of the alloy, the presence of oxygen (bonded in oxides or hydroxides) and carbon (bonded in carbonates) seems to be the most important factor for the resulting corrosion behaviour. The obtained results of the performed analyses are shown in Fig. 4. As can be determined from the peak areas of the measured spectra, carbon content decreased in the following order Zn-0.8Mg-0.2Sr (60%) > Mg_2Zn_{11} without Ar^+ sputtering (43%) > Mg_2Zn_{11} with Ar^+ sputtering (17%) while the oxygen possessed the opposite trend (20% < 32% < 43%). In addition, the ratio between Zn and Mg (Zn/Mg = 1:1 and 1:2, respectively) was not in good agreement with the composition of the individual phases of the material, suggesting an increase in the Mg content in the compounds on the material surface. It was found that the as-cast Mg_2Zn_{11} phase was slightly contaminated by hundredths of percent of calcium, which led to two possible interpretations of C 1s peak at 291 eV binding energy. This peak could be attributed to $CaCO_3$ or $MgCO_3$; however, the minimal relative shifts limits our ability to distinguish individual compounds. The preferential occurrence of $MgCO_3$ could be expected due to the higher concentration of Mg in the

alloy as well as on the material surface (Zn/Mg ratio). O 1s peaks at the binding energies 531 and 533 eV could be assigned to oxides, hydroxides as well as carbonates. In the case of the Mg_2Zn_{11} phase without the sputtering, only about 40% of O 1s intensity belonged to carbonates (based on CO_3^{-2} stoichiometry). In addition, the sputtering led to a decrease in the oxygen contained in carbonates to 25%. This was most likely caused by the removal of elemental contamination, which led to a change in the percentage of the individual elements. The rest of the O^{-2} content was, with high probability, present in the form of Zn/Mg oxides, or hydroxides, or more complex compounds. In the case of Zn-0.8Mg-0.2Sr alloy, the content of oxygen in carbonates could not be determined reliably, especially due to the low value of XPS intensity. This was most likely caused by a high content of adventitious carbon or by the predominant presence of CO_3^{-2} in the intermetallic areas.

In addition to the aforementioned measurements, the distribution of the potentials and the topography of the surface were characterized across the material surface using AFM-KPFM. Characterization of the materials in this way is crucial, especially in the case of localized corrosion attack. The results obtained by AFM-KPFM are shown in Fig. 5. As can be seen in Fig. 5a, Mg-based intermetallic phases were slightly etched after the polishing process. Differences in height between the Zn matrix surface and the bottom of the etched intermetallic particles reached approximately 50 nm. However, small areas with a substantial increase in depth were also observed (Fig. 5a). Beside the intermetallic phases, the grain boundaries were affected before exposure as well. It can be seen in Fig. 5a that the difference in height reached almost 35 nm suggesting relatively significant influence of grain boundaries on the localized corrosion attack during sample polishing. Fig. 5b shows the distribution of the contact potential difference. The highest potential difference was observed in the regions occupied by Mg-based intermetallic phases (90 mV, Fig. 5b with line profile 1) and Zn grain boundaries (30–60 mV, Fig. 5b with line profile 2). Based on the potential scale, the differences between the Zn matrix and the Mg-based intermetallic phases ranged between 100 and 200 mV. It is important to note that the Sr-based intermetallic particles were not reliably distinguishable, and the impact of these particles on the activity of microgalvanic cells will only be discussed based on the available literature.

3.2. Electrochemical measurements

After the initial stabilization, the open circuit potential ranged from −0.88 to −0.92 V/SSCE with constant fluctuations in the range of millivolts for all measurements. The polarization resistance values were 5.1 ± 1.2 kΩ.cm2. Several different areas are visible on the potentiodynamic polarization curves (Fig. 6). The anodic curve showed a clear change of slope at a potential of −0.73 V/SSCE, above which the curve reached the standard progression of the active corrosion mechanism with subsequent limit diffusion control of the reaction; however, even the Tafel slope below this potential with a value of 0.075 V/decade did not point towards passivation behaviour. In the area adjacent to the EOCP, the Tafel slope reached 0.131 V/decade. Furthermore, a number of waves appeared in the cathodic region, the first wave belonging to the dehydrogenation of hydrogen phosphate and the others have been identified in the past, in an environment aerated with 1 M NaCl, as - ZnO, (Zn(OH) 2), Zn(OH)2 · ZnCl2, and Zn(OH)2 · ZnCl2 (in order of decreasing potential) [52,53]. The last wave already corresponded to hydrogen depolarization.

Fig. 7a and 7d show a Nyquist presentation of impedance data obtained during the exposure. It is clear from the shape of the spectra that the data did not form a regular semicircle, so there was a clear influence of the second time constant in the spectrum. The spectra were modeled by the equivalent circuit shown in Fig. 7b and the results (extended by the EOC) are summarized in time evolution graph in Fig. 7c. The equivalent circuit consisted of a resistor Rsol describing the resistivity of the solution and a semi-parallel arrangement of two-time constants. The constant phase element (CPE) used in the circuit generally substituted
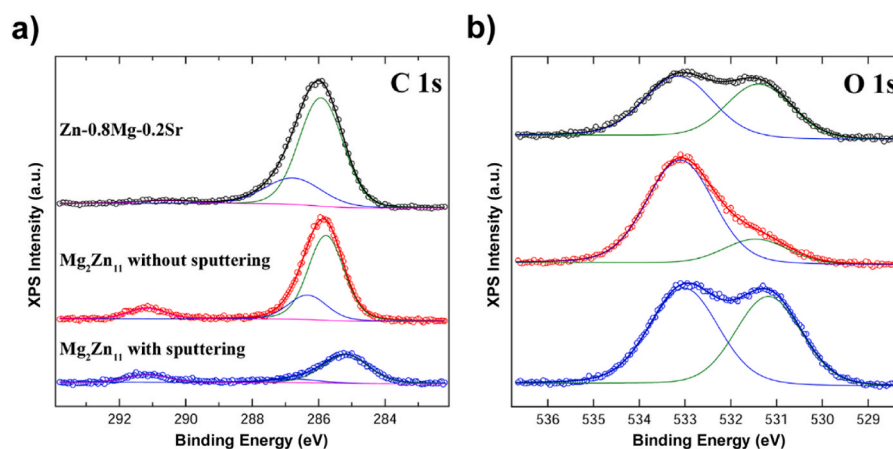
Table 2
Bulk composition of the zinc matrix from the mid-lower right hand section of the tip shown in Fig. 3.

Ion	Count	Concentration (at. %)	Concentration (wt. %)
Zn	8304974	99.973	99.970
Mg	195	0.002	0.001
Sr	1380	0.017	0.023
Fe	649	0.008	0.007

Fig. 4. Sections of XPS spectra concerning a) C 1s and b) O 1s peaks of the Zn-0.8Mg-0.2Sr alloy (black line), Mg_2Zn_{11} phase without the sputtering (red line) and Mg_2Zn_{11} phase with the sputtering (blue line).
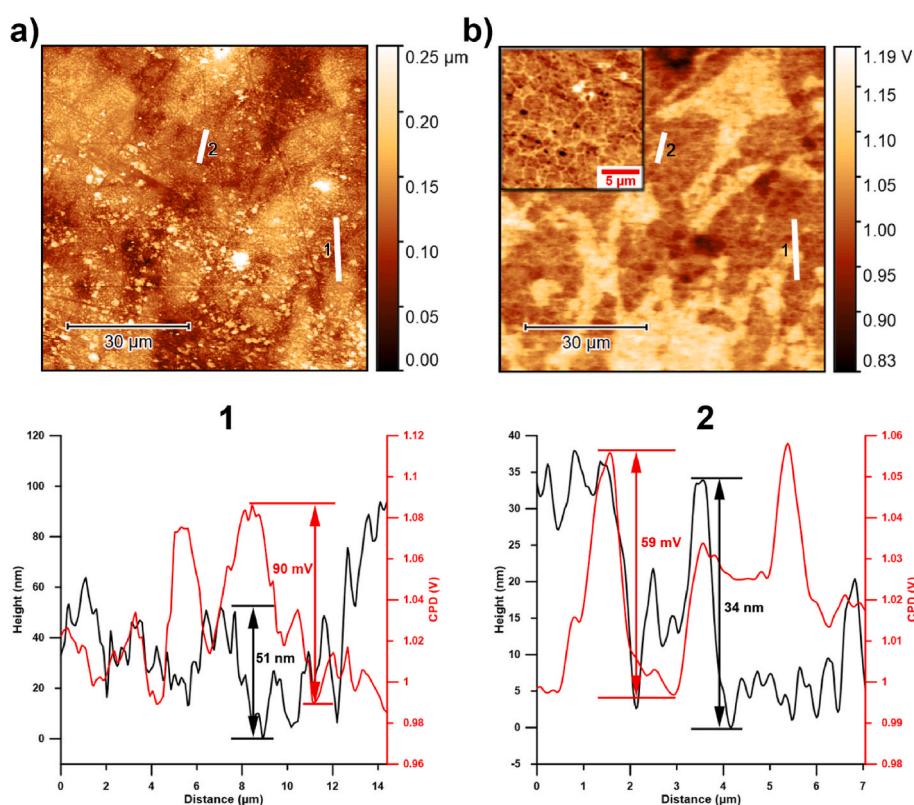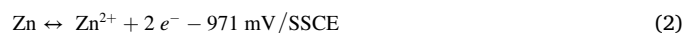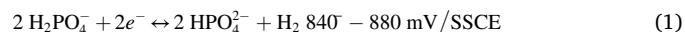

Fig. 5. a) Topography and b) contact potential difference (CPD) with detail of grain boundaries of Zn-0.8Mg-0.2Sr surface and two line profiles of selected areas representing the transition between zinc matrix and intermetallic phases (1) and transition between individual Zn grains (2).

the capacitor and this replacement reflected the non-ideal behaviour of the system. This element was defined as $Z = [C(j\omega)\,\alpha\,]^{-1}$, where alpha took values from 0 to 1, so it can reflect from purely resistive to fully capacitive behaviour. Capacitance of the element was calculated according to Brug et al. [54]. Throughout the exposure, the outer surface showed a dominant capacitive character and was described by a CPE. The charge exchange was realized to be locally dominant (in the pore) and was strongly influenced by transport processes, which was reflected by the presence of the Warburg element in the equivalent circuit. The experimental curves and used circuit showed a high level of consistency, expressed as values of χ^2 lower than $1{\bullet}10^{-4}$. The EOC values in the first part of the exposure indicated a mixed response controlled by reactions:

$$2\,H_2PO_4^- + 2e^- \leftrightarrow 2\,HPO_4^{2-} + H_2 \quad 840^- - 880\ mV\big/SSCE \tag{1}$$

$$Zn \leftrightarrow Zn^{2+} + 2\,e^- \quad -971\ mV\big/SSCE \tag{2}$$

while it was noticeable that at the 52nd hour of exposure there was a sharp transition to **Eq. (2)** only, followed by a return to the mixed control. The slight fluctuations are influenced both by the measurement of the impedance spectra and by other ongoing reactions - the influence of dissolved Zn^{2+} concentrations by the formation of solid corrosion products and also by the competition of oxygen depolarization and the reaction **Eq. (1)** (phosphates dehydrogenation [55]. Significant decrease in potential was reflected in the impedance spectra (green
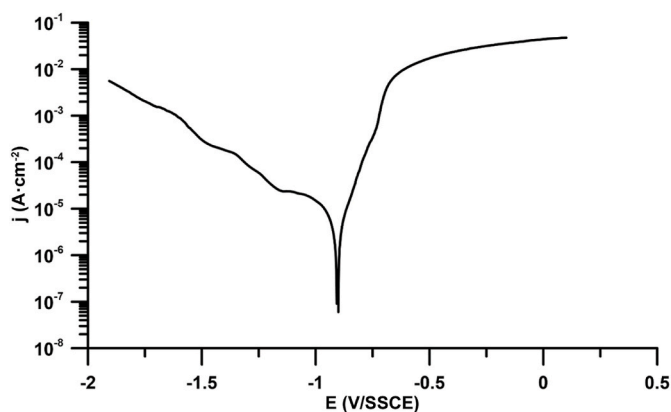
Fig. 6. Polarization curves in SBF.

curves in Fig. 7d), with an increase in the admittance of the Warburg element, an increase in the resistance parallel to it, a decrease in the upstream resistance, and an increase in the capacitance of the outer surface. These changes indicated a significant localization of the charge exchange and thus the formation of several preferentially corroding sites.

3.3. Immersion tests

Initiation of the corrosion attack was clearly visible on 3D and 2D images obtained by micro-CT, and the results concerning these measurements are shown in Fig. 8. As can be seen in Fig. 8a (0 h of exposition), the areas of the intermetallic phases containing Mg_2Zn_{11} and $SrZn_{13}$ were characterized by darker shades, and the phases were separated by bright areas representing zinc matrix. It is visible that the gradual increase of exposure time led to an increase in surface damage. This led to a gradual decrease of material volume and increase of surface area. In the beginning stage of the exposition, the corrosion attack was localized predominantly to the areas containing intermetallic phases. With subsequent increase of time exposure, the number of attacked regions adjacent to intermetallic phases increased, and the first signs of localized corrosion attack were visible in Fig. 8c. After 72 h of exposure (Fig. 8d), regions without corrosion attack (containing the intermetallic phases) were observed on the material surface as well. It suggests the presence of non-affected areas, and that development of the corrosion attack is limited to the expansion of existing local corrosion areas. The observations of 2D images after 72 h of exposure confirmed corrosion processes dominated by the spreading of the corrosion front along the intermetallic phases. In addition, the maximal depth of the corrosion attack was determined using 2D scans in the y axis (details in the supplementary materials). The values of maximal depth were 12 μm, 25 μm and 39 μm for 24 h, 48 h and 72 h, respectively. To confirm the character of long-term behaviour, immersion tests were performed for 14 days with subsequent characterization of the corroded material.

Distribution, elemental composition, and morphology of the corrosion products formed during the immersion in SBF for 72 h and 14 days are shown in Fig. 9. The overview image after 72 h of exposure showed macroscopic deposits in localized places (Fig. 9a). A close-up view of the surface (Fig. 9b) showed dimples with geometries corresponding to the intermetallic phases. The presence of a thin layer of corrosion products was also evident on the surface, but its thickness did not cover the underlying character of the surface. EDS analysis showed the presence of calcium and phosphorus, but the Ca/P ratio did not exceed the value of 0.3 excluding the presence of compounds solely on the hydroxyapatite base. The EDS spectra also indicated increased content of carbon and oxygen, however, due to the limited ability to quantitatively resolve O and C using EDS [56], this observation was only indicative. Fig. 9c shows a spot after mechanical removal of the deposit where a crevice

was evident, and in which EDS analysis showed an order of magnitude higher chlorine abundance than on the rest of the surface. As can be seen after 14 days exposure (Fig. 9d), the corrosion products were still unevenly distributed over the surface of the sample. Detailed observations revealed the pores character of the corrosion products (Fig. 9d$_1$), and the presence of Zn, O, Cl, P, and Ca (with the same distribution as P) were confirmed by EDS analysis. To describe the extent of the corrosion attack, the corrosion products were chemically removed from the material surface (Fig. 9e). It needed to be taken into account that the surfaces of the samples shown in Fig. 9d differ from those in Fig. 9e. The reason for using different surfaces is to enhance the visibility of described facts. Pits caused by the corrosion attack showed relatively high depth (up to 250 μm), and the presence of the crevices on their bottom (Fig. 9e$_2$). On the contrary, the surface of the sample outside the pits showed minimal changes in the morphology and minimal corrosion attack (Fig. 9e$_1$). It also needs to be mentioned that the pH of the corrosion environment increased during the exposition from 7.9 to 8.6. Last but not least, the corrosion rate of the alloy was evaluated using the weight-loss method, and the average value was found to be 0.36 mm·a^{-1}. Additionally, the values of the corrosion rate remained stable in time with standard deviation of ±0.01 mm·a^{-1}.

In addition, the corrosion products were analysed using XRD, TEM, and Raman spectroscopy. The XRD analysis revealed the presence of simonkolleite ($Zn_5(OH)_8Cl_2$·H_2O, minority (1–10%)) and hydrozincite ($Zn_5(CO_3)_2(OH)_6$, majority (90–99%)), which are the most common corrosion products of Zn-based materials exposed to SBF [57–59]. The presence of compounds containing other alloying elements (Mg, Sr) were not confirmed by XRD. Selected area electron diffraction (SAED) analysis confirmed only the presence of hydrozincite (Fig. 10). In addition, STEM - EDS indicated the presence of low amounts of simonkolletite and phosphate-based compounds (Fig. 10c, point 2). Raman measurements were in good agreement with XRD and TEM measurements, where the hydrozincite and simonkolleite were identified as corrosion products. For details concerning the XRD analysis and Raman spectroscopy, please see the supplementary materials.

Ion release of zinc, magnesium, and strontium was measured immediately after exposure to SBF using AAS, the obtained results are summarized in Table 3. The samples for the AAS measurements were extracted by two different methods: i) extraction from the top of the container (i.e. medium without the sediments) and ii) extraction from the acidified solution containing dissolved sediments (see the experimental section). This procedure revealed that the concentrations of magnesium and strontium ions were almost the same independently of the place and method of the extraction. However, small differences can be observed between these values suggesting partial bonding of Mg and Sr into the solid sediments. In contrast, the content of zinc ions was significantly higher after the acidification of the solution (dissolution of the sediments). It means that the solid corrosion deposits contained a large amount of zinc and only a negligible or even no amount of magnesium or strontium.

4. Discussion

Description of the material microstructure and surface composition clearly shows the complex character of the system and pointed to several factors that can affect the resulting corrosion behaviour of zinc-based alloys. These factors can be divided into three basic groups: i) distribution and nobility of the intermetallic phases, ii) grain size and the chemical composition of the grain boundaries, and iii) protective character of native layers formed on the surface before the exposition. It needs to be mentioned that the literature sources supporting the claims and discussion in the manuscript was limited based on the relevance and not time period. Due to the longer time period, the information can be obtained from many sources dealing with different aspects of the solved problematic, thereby covering all knowledge related to the issue.

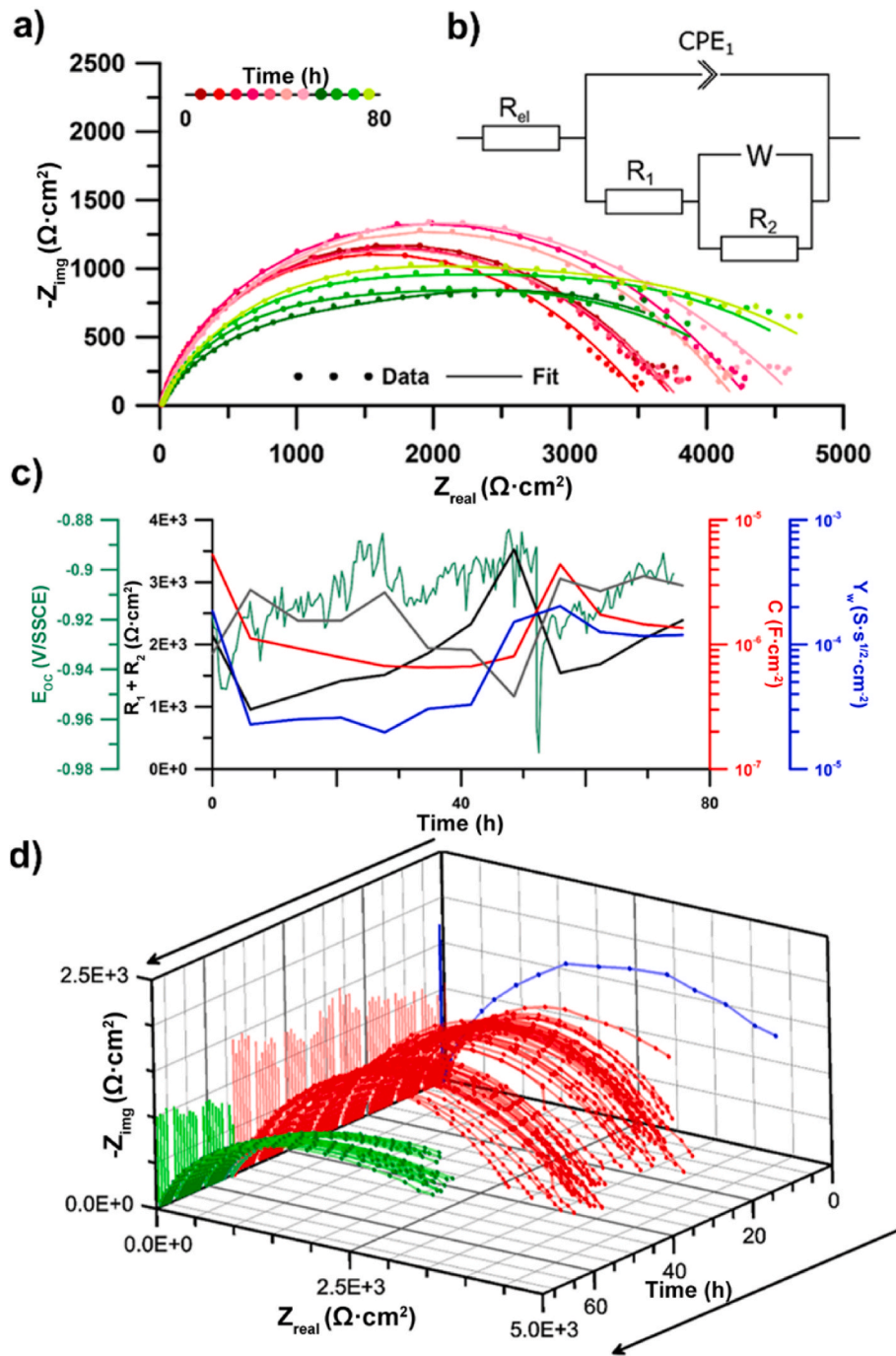i) It is well known that the solubility of the alloying elements (Mg, Sr)

Fig. 7. a) Fitted extended impedance spectra in SBF; b) equivalent circuit used for evaluating impedance measurement; c) time evolution of circuit elements d) detailed time evolution of the impedance response at mid frequencies.

in Zn solid solution at ambient temperature is very low. This can be clearly visible in the Zn-Mg [60] and Zn–Sr [60] phase diagrams, where the solubility of these elements in Zn reach the values close to zero. Therefore, the preferential binding of these elements into intermetallic phases takes place during the solidification of the material [61]. Moreover, the difference in the solubility of Mg and Sr in Zn at the solidification and ambient temperature is very low. As a consequence, only limited number of precipitates inside the Zn grains are formed during the cooling between the solidification and ambient temperature. This was also confirmed by the APT measurements, which have shown almost negligible content of the alloying elements in the Zn matrix and a very limited number of precipitates. Distribution of the intermetallic

phases can be described as homogeneous in large scale, and it was strongly affected by the material processing. However, the opposite situation can be observed in local arrangements (Fig. 2a). The local inhomogeneity can be ascribed to the initial state of the material prior to processing, where the zinc dendrites were surrounded by the intermetallic phases [34]. The ECAP processing leads to the disruption of these areas and the formation of a large number of smaller intermetallic particles [34]. These particles serve as the initial places for corrosion attack. The intermetallic particles possess lower nobility (Fig. 5b) compared with the zinc matrix, resulting in the occurrence of local galvanic cells. The results obtained in this study reveal two different mechanisms, which are strongly dependent on the exposed areas. On
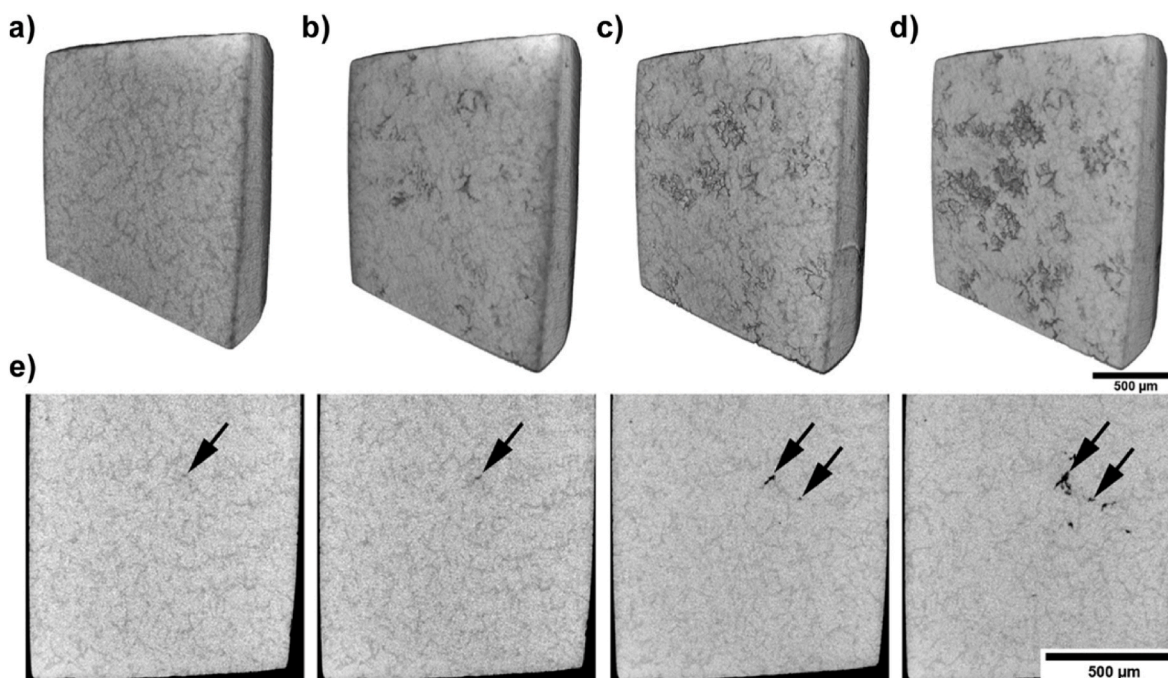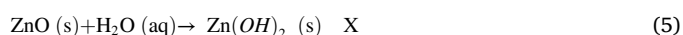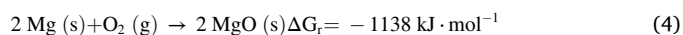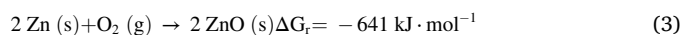
Fig. 8. 3D scans of the sample exposed in SBF for a) 0 h, b) 24 h, c) 48 h and d) 72 h with e) 2D slides representing gradual corrosion attack spreading along the intermetallic particles (marked by the arrows).

one hand, the intermetallic phases caused an increase in the speed of corrosion attack because of their lower nobility [32,62]. On the other hand, the phases participate on the changes in chemical composition of the surface through the formation of MgO and MgCO$_3$, which positively affected the corrosion resistance [63]. This will be further discussed in the following paragraphs. In addition, the complex character of the intermetallic areas can affect the corrosion process by changes of the ratio between zinc areas and Mg$_2$Zn$_{11}$ phases. More precisely, the corrosion attack can be affected by a mutual ratio between cathode and anode size.

ii) It is well known that the grain size can significantly influence the corrosion rate of a material. This fact is often ascribed to the ability of grain boundaries (GB) to effectively aid in the formation of a passivating oxide layer [64]. Therefore, the grain boundary density could be expected to influence the corrosion rate of the material. Ralston et al. [64] found a correlation between GB density and corrosion rate of "reactive" materials (i$_{corr}$ > 10 µA cm^{-2}). In such cases, high grain boundary density leads to an intensification of the corrosion process by increasing surface reactivity. It means that in the case of our material, the areas containing non-recrystallized grains should be more resistant against the corrosion attack than the fine-grained areas, and thus support non-uniform corrosion attack. Another important aspect connected with grains is the chemical composition at the grain boundaries. As can be seen from results obtained by KPFM, the grain boundaries possessed lower potential compared to the matrix. Lower potential can lead to the predominant etching of the grain boundary with subsequent intensification of the corrosion attack in these regions. This situation can be caused by several factors including the magnesium segregation, the energy of the GB, or a combination of the two. It is well known that grain boundaries possess higher internal energy due to different arrangement of the atoms compared with the bulk [65]. According to the combined statements of the first and second law of thermodynamics, internal energy is directly proportional to Gibbs energy. Furthermore, the Gibbs energy is equal to negative value of potential suggesting the participation of grain boundary structure on the decrease of potential value. Besides, the presence of segregated less noble Mg must have similar impact on the potential value on the GB. However, the content of Mg is

relatively low (0.3 at. %), suggesting a prevailing influence of GB energy on the overall potential difference between grain boundaries and Zn matrix.

iii) Kinetics of layer formation is an important factor in Zn–Mg$_2$Zn$_{11}$ systems, influencing the corrosion resistance of the material. In the case of the studied material, the competition between MgO and ZnO layers could be expected on the intermetallic particles. The protective character of Mg-based oxides and their formation was discussed in several publications concerning the influence of Mg$_2$Zn$_{11}$ on the corrosion properties of Zn–Mg$_2$Zn$_{11}$ systems [26,36,66,67]. The reason lies in the presence of MgO which often leads to the formation of a layer with a more protective character (compared to ZnO) and increases corrosion resistance. However, such behaviour relates to the kinetics of oxide growth and to the suitable conditions for the creation of a homogeneous layer. At the micro-scale, the distribution of the Mg-based phase is inhomogeneous, and the conditions for the creation of compact oxide layer are not reached. As a result, non-uniform corrosion attack could be expected. According to the obtained results, a mixture of oxides, hydroxides, and carbonates are expected on the material surface. However, such a large group of possible corrosion products is not suitable for further investigation due to their different protective character. In order to understand the kinetics, the group of compounds forming on the material surface before the exposure (Eq. 3–9) were thermodynamically restricted. The raw data for the calculations of Gibbs energies (ΔGr) were obtained from literature [68–70]. As determined from the equations, the presence of oxides and carbonates is the most probable result. Together with the XPS results, the material surface is, with high probability, covered by oxides (ZnO – matrix and MgO – intermetallic regions) and magnesium carbonate, and the stability of individual compounds increased in the following order: ZnCO$_3$ < Mg(OH)$_2$ < MgCO$_3$ < ZnO < MgO. The presented claims corresponded with the thermodynamic calculations and obtained experimental results [71].

$$2 \text{ Zn (s)} + \text{O}_2 \text{ (g)} \rightarrow 2 \text{ ZnO (s)} \quad \Delta G_r = -641 \text{ kJ} \cdot \text{mol}^{-1} \tag{3}$$

$$2 \text{ Mg (s)} + \text{O}_2 \text{ (g)} \rightarrow 2 \text{ MgO (s)} \quad \Delta G_r = -1138 \text{ kJ} \cdot \text{mol}^{-1} \tag{4}$$

$$\text{ZnO (s)} + \text{H}_2\text{O (aq)} \rightarrow \text{Zn}(OH)_2 \text{ (s)} \quad X \tag{5}$$
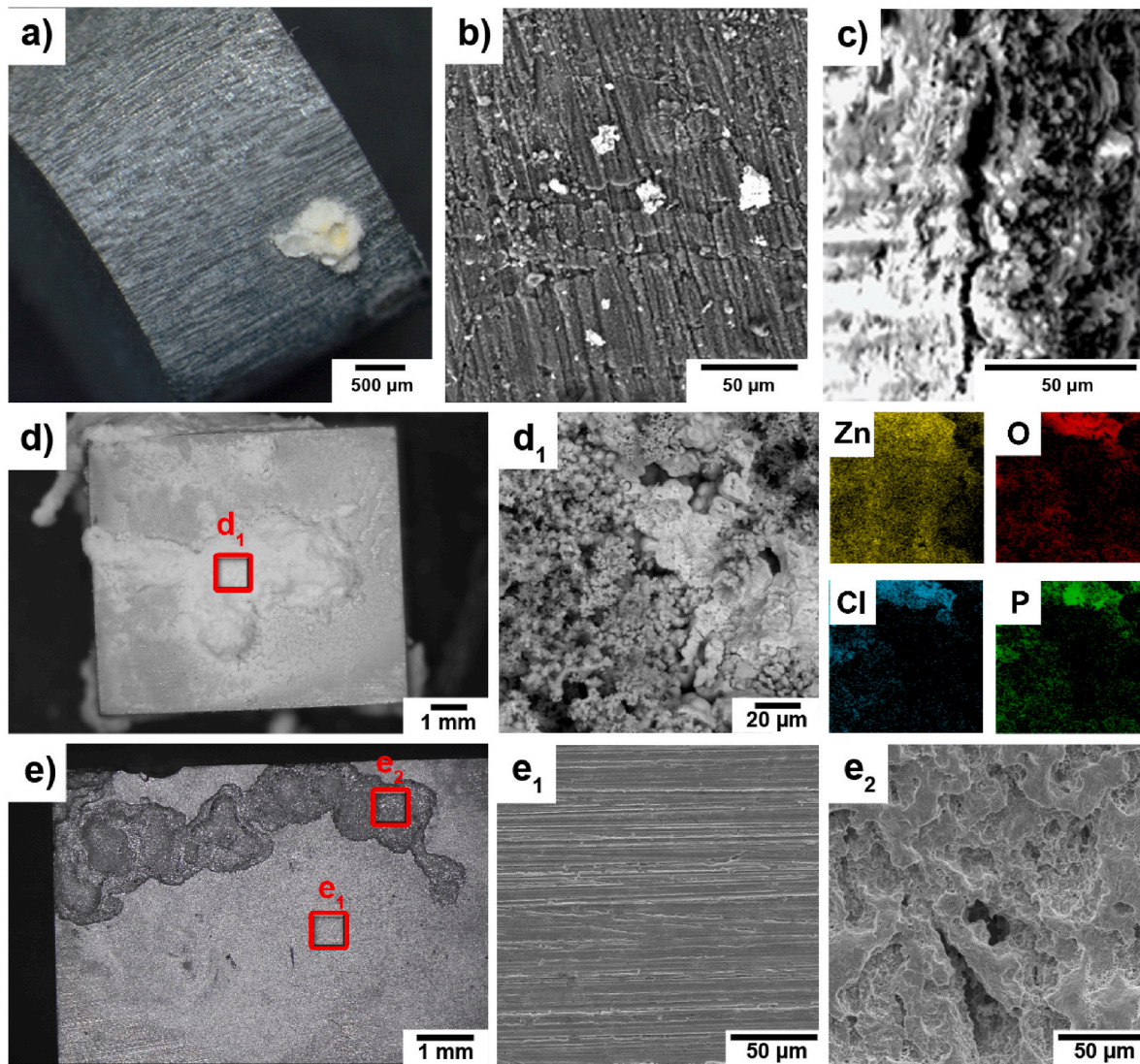
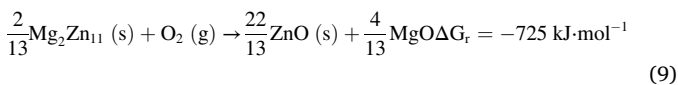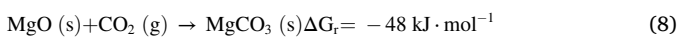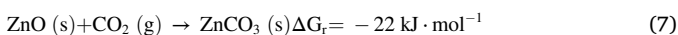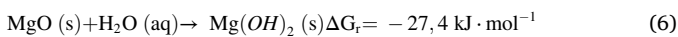**Fig. 9.** LM and SEM images of as-ECAPed Zn-0.8Mg-0.2 Sr alloy a) after the 72 h of exposition with b) detailed images of etched intermetallic regions and c) crevice created under the corrosion products; d) samples after the 14 day exposure in SBF solution with d_1) elemental maps of the corrosion products; e) surface of the alloy after the chemical removal of the corrosion products with detailed images of the e_1) non-attacked surface and e_2) bottom of the pits.

$$MgO \; (s) + H_2O \; (aq) \rightarrow \; Mg(OH)_2 \; (s) \Delta G_r = -27,4 \; kJ \cdot mol^{-1} \qquad (6)$$

$$ZnO \; (s) + CO_2 \; (g) \; \rightarrow \; ZnCO_3 \; (s) \Delta G_r = -22 \; kJ \cdot mol^{-1} \qquad (7)$$

$$MgO \; (s) + CO_2 \; (g) \; \rightarrow \; MgCO_3 \; (s) \Delta G_r = -48 \; kJ \cdot mol^{-1} \qquad (8)$$

$$\frac{2}{13}Mg_2Zn_{11} \; (s) + O_2 \; (g) \rightarrow \frac{22}{13}ZnO \; (s) + \frac{4}{13}MgO \Delta G_r = -725 \; kJ \cdot mol^{-1} \qquad (9)$$

All the mentioned effects lead to the prediction of a non-uniform corrosion attack; however, it is not possible to determine the prevailing aspect only based to the microstructural characterization. It is obvious that the mentioned factors (intermetallic phases, grain size and boundaries, layers formed before exposition) affect the corrosion behaviour of the material the most; however, other less significant aspects, such as internal stresses or texture could participate in the corrosion process as well [72,73]. This is relevant, especially in the case of materials processed by thermomechanical or severe plastic deformation processes. Based on the performed measurements and the lower significance of these features, the influence of the texture and internal stresses will not be further discussed in this manuscript. Until now, the discussion was focused predominantly on the influence of Mg dissolved in material and the Mg-based intermetallic phases on the corrosion behaviour of the ECAPed material. The reason for such restriction was caused by the microstructural arrangement and the possibility to confirm our assumptions reliably. Alongside the Mg-based intermetallic phases, $SrZn_{13}$ particles were also present. The primary reason for adding Sr was to enhance the ductility of the alloy [32]. As demonstrated in our previous study [34], the $SrZn_{13}$ phase content (3.2 vol %) was significantly lower than that of the Mg_2Zn_{11} phase (14.8 vol %). Furthermore, the $SrZn_{13}$ particles were very small (less than 1 μm) and occurred together with the Mg_2Zn_{11} particles. Thus, their impact on the localization of corrosion was not noticeable. Additionally, no grain boundary segregation of Sr or Sr-enriched surface layers were observed. These findings suggest that the effect of Sr on the corrosion mechanism can be disregarded in our case. However, the influence of these particles on the corrosion mechanism has been documented in literature for binary Zn–Sr alloys and is primarily related to the activity of micro-galvanic cells, where these phases increase anodic activity [27]. The expected potential decrease is well supported by brighter places in the intermetallic particles visible in Fig. 5.

Exposure tests augmented by the impedance analysis and in-situ micro-CT followed by surface analysis showed preferential corrosion
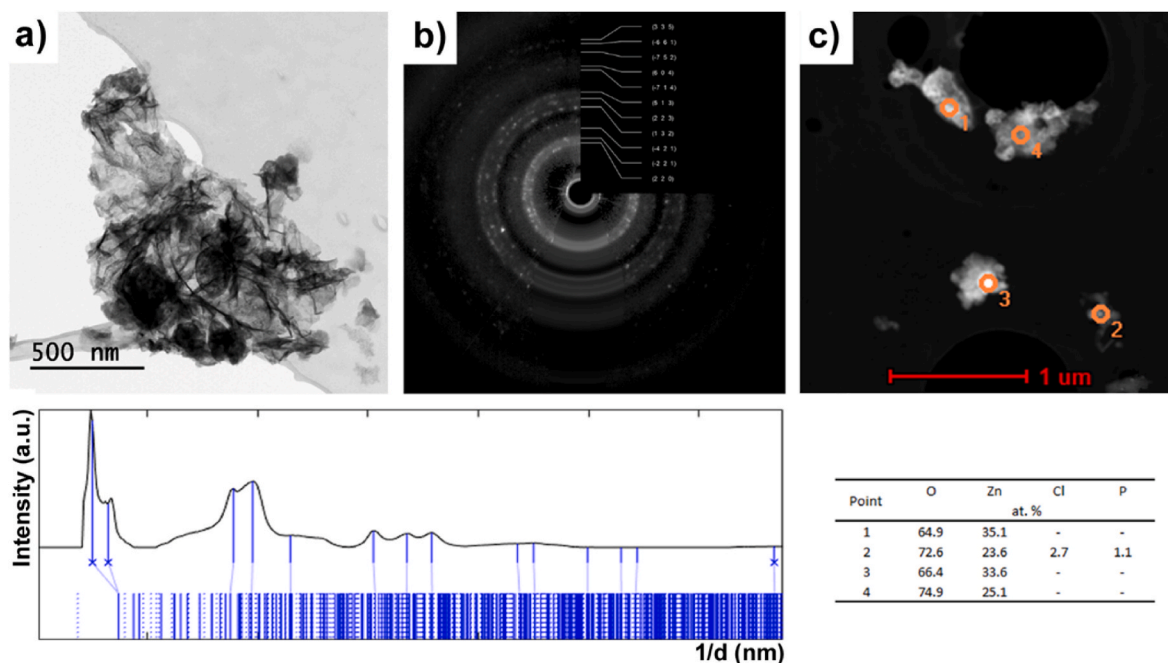
Fig. 10. a) TEM images of the corrosion products supplemented by b) selected area diffraction pattern with the marked lines belonging to of hydrozincite; c) elemental point analysis of selected particles with table summarizing the elemental composition in at. %.

Table 3
Ion release of the individual elements determined by different approaches using AAS method (mg·L^{-1}) with calculated concentrations from weight loss.

Day	Medium without sediments			Medium with dissolved sediments			Calculated concentration (weight loss)			Corrosion rate	SBF		
	Zn	Mg	Sr	Zn	Mg	Sr	Zn	Mg	Sr	mm·a^{-1}	Zn	Mg	Sr
2	0.33	25.1	0.07	2.50	25.90	0.06	17.40	0.14	0.04	0.36	0.03	24	0.06
5	0.43	25.7	0.09	9.11	27.60	0.09	25.14	0.20	0.05	0.32			
7	0.43	26.1	0.08	12.00	29.10	0.11	67.68	0.55	0.14	0.37			
9	0.68	25.9	0.08	10.80	28.10	0.10	79.28	0.64	0.16	0.36			
12	2.05	28.7	0.11	13.80	30.90	0.12	129.55	1.05	0.26	0.38			
14	1.25	29.3	0.11	17.10	32.30	0.13	143.09	1.16	0.29	0.37			

Error of measurement in the range of 0–5%.

of the intermetallic phases in the first stages of exposure. Dehydrogenation of the dihydrogen phosphate contributed to the partial phosphate character of the barrier layer protecting most of the surface. The Ca/P ratio excludes the formation of products purely on the apatite base and indicates the presence of zinc phosphate compounds. However, their content is relatively low suggesting the predominant binding of zinc ions into simonkolleite and hydrozincite. Subsequently, the content of chlorides increased in some selected pores due to the crevice corrosion mechanism leading to the acceleration of the localized attack. Besides the character of the corrosion attack, the composition and stability of newly formed products during the exposure are important, especially from the biodegradable implant's point of view. Most of the corrosion products consisted of hydrozincite and simonkolleite. These compounds are relatively common in the case of zinc exposed in the solutions containing the Cl$^-$ ions [57,74,75]; however, their mutual ratio is often different, and it is dependent on many factors from which the pH and the presence of other compounds seem to be the most important. It is known that simonkolleite is more stable at lower pH, while formation of hydrozincite is preferred in more alkaline environments [63]. This points to the initial formation of simonkolleite with a gradual increase of hydrozincite during the exposure and with an increasing pH value. In addition, the formation of hydrozincite could be supported by the presence of magnesium carbonate suggesting the predominant formation of hydrozincite in the areas occupied predominantly by intermetallic phases [63]. XPS results also confirmed higher content of

magnesium on the material surface compared with the Zn: Mg ratio in the intermetallic phases. All these results together with the gradual increase in pH value led to a higher content of hydrozincite in the resulting corrosion products. The importance of such a conclusion is hidden in the stability of simonkolleite, which is relatively stable in a neutral pH environment, and it could result in a decrease in the degradation rate in the human body after implantation. Despite the ability of the body to keep a stable pH value, an increase of pH could be expected in the close surrounding of the material surface resulting in similar results as in the presented work. Simplified schema of the corrosion process in the individual stages is shown in Fig. 11.

Despite some differences, similar conclusions as in this study can also be found in our previously published manuscripts concerning *in vivo* behaviour of the as-extruded Zn-0.8Mg-0.2Sr alloy [76,77]. The materials were processed in different manners (extrusion vs. ECAP); however, it led only to a different arrangement of the intermetallic phases while the composition and zinc grain size remained approximately the same. Because of that, a comparison between these experiments is possible, and allows us to reveal the differences and similarities among them. First of all, the corrosion process spread along the intermetallic phases meaning that localized corrosion attacks take place in both cases. Additionally, the corrosion rate was significantly lower in the living organism compared to the presented results obtained by *in vitro* tests (13.5 µm y^{-1} vs. 290 µm y^{-1}, respectively). The reason for such behaviour can be attributed to the presence of proteins and enzymes
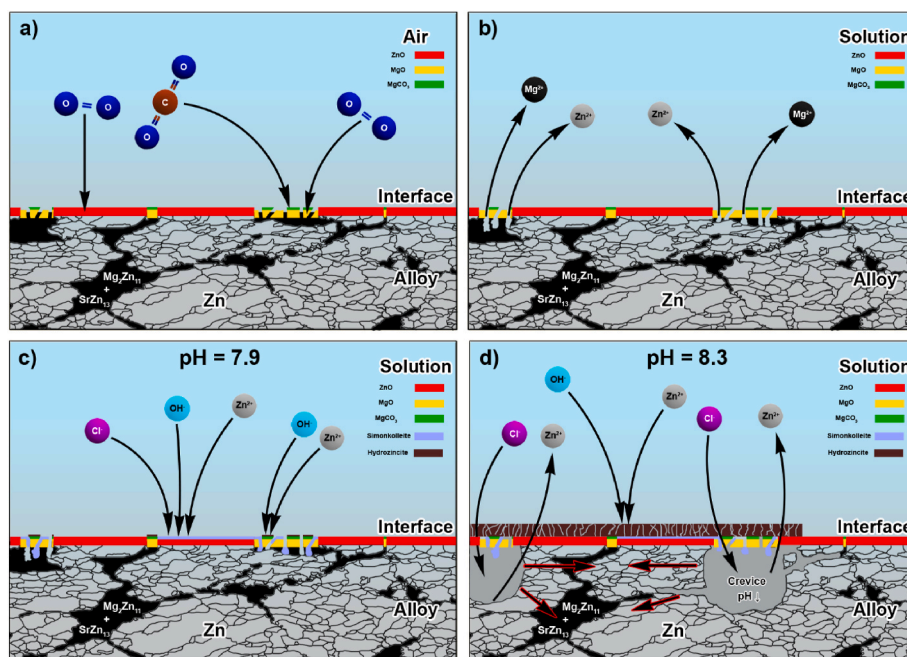
Fig. 11. Simplified schema of the corrosion mechanism and behaviour in the individual stages of exposure of the sample a) before exposure (the reactions took place in the thin layer of water-based electrolyte), b) after 72 h exposure, c) with the presence of simonkolleite and d) at the end of the 14 day exposure.

under *in vivo* conditions. It is obvious that the presence of these organic compounds can increase the corrosion rate by binding zinc ions into complexes during the initial stages of exposure (disruption of the system equilibrium). After a certain amount of time, the formed complexes often cover the implant's surface, forming a barrier of corrosion products that protect the surface [78,79]. This process leads to a significant decrease in the corrosion rate. However, these general conclusions can differ based on the type of organic compound and pH in the implant's surroundings. Because of that, it is quite challenging to predict the exact influence of individual compounds on the implant's corrosion behaviour. The released ions did not cause any adverse effects *in vivo*. The amount of Zn^{2+} ions released per day (approximately 18.4 μmol L^{-1}) obtained in this study was low enough to be tolerated by various cells commonly used for viability tests concerning biodegradable Zn alloys [80–82]. The value is also significantly lower compare to the recommended daily allowance for zinc [83], excluding the complications such as zinc-induced copper deficiency. As was mentioned, even lower corrosion rate is expected, and higher biocompatibility should be observed *in vivo* than *in vitro*. This suggests that the investigated material should be safe for the fabrication of implants with a large surface area from the corrosion and biocompatibility point of view.

In addition to the corrosion mechanism, the stability of the mechanical properties during the degradation is crucial for the applicability of biodegradable alloys as well. In the case of zinc, several factors can affect its mechanical behaviour, such as recrystallization, natural aging or localized corrosion attack. Recrystallization of pure zinc starts around −12 °C, indicating the possible changes in the material's microstructure caused by elevated temperatures (37 °C) [84]. Furthermore, the mechanical behaviour can be significantly affected by localized corrosion attack, where surface changes lead to stress concentration. Both recrystallization and local corrosion attack can cause a significant decrease in mechanical properties and result in failure of the material's functionality. Therefore, it is necessary to determine the time and cause of the decrease in mechanical properties. However, such a description of the process is a relatively complex problem and requires a detailed separate study to obtain reliable results. On the contrary, the impact of mechanical loading on corrosion behaviour can also be discussed. During the loading of the implant, the formation of cracks in a direction

perpendicular to the loading direction can be expected. The dimensions of these cracks can affect the corrosion rate through effectiveness of the ion transportation. However, the process of ion transportation is affected by frequency of loading as well [85]. At lower frequencies, the time for ion transportation from the crack is sufficient, and the significance of the corrosion damage increases. Conversely, higher frequencies do not allow the transportation of ions, resulting in predominant mechanical damage. In the case of the implants, lower frequency of the loading could be expected. Because of that, the intensification of the corrosion process can be expected by the simultaneous activity of the corrosion environment and mechanical loading [85,86]. Within this study, we investigated the evolution of the mechanical performance during a time period of only 14 days. In this short period simulating the initial stage after the implantation, no significant changes in mechanical behaviour were observed. For more details, please, see the supplementary data.

5. Conclusion

In this study, corrosion mechanism of the as-ECAPed Zn-0.8Mg-0.2Sr alloy was proposed and described and the findings arising from this publication can be summarized into the following points.

1) The surface of the sample was partially covered by very thin layers of ZnO, MgO, and MgCO$_3$ before exposure to SBF. These compounds were unevenly distributed over the surface of the sample with initiation of oxidation occurring at intermetallic phases. The layers, which naturally form on the material possessed different resistance to corrosion attack and support the subsequent localized corrosion mechanism.
2) The segregation of Mg on the grain boundaries increased the potential difference between the zinc matrix and the boundaries.
3) In the initial stages of the exposure in the SBF solution, the intermetallic regions were predominantly etched and the Zn^{2+} and Mg^{2+} ions were released into the solution. Ions released in this way were subsequently bonded into solid corrosion products or sediments.
4) Simonkolleite and hydrozincite with minor amounts of $Zn_x(PO_4)_y$ were identified as the corrosion products. The porous character of corrosion products was also observed.

5) The presence of crevice corrosion mechanism was confirmed by SEM and EIS.

Besides these findings, the comparison with the *in vivo* tests suggest the usability of these materials from the degradation point of view. The knowledge obtained in this manuscript can be almost fully applied to many biodegradable Zn–Mg-based alloys containing low amount of third element less noble than Zn matrix (alloys containing Mg and Ca, Sr or Li). The type of thermomechanical treatment should play no significant role on the corrosion behaviour as well. It is true that different chemical composition and method of thermodynamical treatment can lead to differences in microstructure (distribution of intermetallic phases, grain boundary segregation, grain size and texture) and the corrosion behaviour could slightly differ in various Zn–Mg based materials. Despite that, the main trends concerning the corrosion mechanism should be preserved.

Ethics approval

I declare that.

1. The article is original.
2. The article has been written by the stated authors who are ALL aware of its content and approve its submission.
3. The article has not been published previously
4. The article is not under consideration for publication elsewhere
5. No conflict of interest exists, or if such conflict exists, the exact nature must be declared.
6. If accepted, the article will not be published elsewhere in the same form, in any language, without the written consent of the publisher.

CRediT authorship contribution statement

Jan Pinc: Conceptualization, Methodology, Formal analysis, Investigation, Data curation, Writing – original draft, Visualization. **Andrea Školáková:** Investigation, Writing – review & editing, Formal analysis. **Vojtěch Hybášek:** Investigation, Writing – original draft, Visualization. **Šárka Msallamová:** Investigation. **Petr Veřtát:** Investigation, Formal analysis. **Petr Ashcheulov:** Investigation, Formal analysis. **Martin Vondráček:** Investigation, Formal analysis. **Jan Duchoň:** Investigation, Formal analysis. **Ingrid McCarroll:** Investigation, Formal analysis, Writing – review & editing. **Matěj Hývl:** Investigation, Formal analysis. **Swarnendu Banerjee:** Investigation, Formal analysis. **Jan Drahokoupil:** Investigation, Formal analysis. **Jiří Kubásek:** Investigation, Writing – review & editing, Funding acquisition. **Dalibor Vojtěch:** Investigation. **Jaroslav Čapek:** Writing – review & editing, Supervision.

Declaration of competing interest

None.

Acknowledgement

Appendix A. Supplementary data

Supplementary data to this article can be found online at https://doi.org/10.1016/j.bioactmat.2023.04.012.

References

[1] Y. Liu, Y. Zheng, X.-H. Chen, J.-A. Yang, H. Pan, D. Chen, L. Wang, J. Zhang, D. Zhu, S. Wu, K.W.K. Yeung, R.-C. Zeng, Y. Han, S. Guan, Fundamental theory of biodegradable metals—definition, criteria, and design, Adv. Funct. Mater. 29 (18) (2019), 1805402.

[2] H.-S. Han, S. Loffredo, I. Jun, J. Edwards, Y.-C. Kim, H.-K. Seok, F. Witte, D. Mantovani, S. Glyn-Jones, Current status and outlook on the clinical translation of biodegradable metals, Mater. Today 23 (2019) 57–71.

[3] M.P. Staiger, A.M. Pietak, J. Huadmai, G. Dias, Magnesium and its alloys as orthopedic biomaterials: a review, Biomaterials 27 (9) (2006) 1728–1734.

[4] F. Witte, H. Ulrich, M. Rudert, E. Willbold, Biodegradable magnesium scaffolds: Part 1: appropriate inflammatory response, J. Biomed. Mater. Res. 81A (3) (2007) 748–756.

[5] G. Chandra, A. Pandey, Biodegradable bone implants in orthopedic applications: a review, Biocybern. Biomed. Eng. 40 (2) (2020) 596–610.

[6] Y.F. Zheng, X.N. Gu, F. Witte, Biodegradable metals, Mater. Sci. Eng. R Rep. 77 (2014) 1–34.

[7] H. Li, Y. Zheng, L. Qin, Progress of biodegradable metals, Prog. Nat. Sci.: Mater. Int. 24 (5) (2014) 414–422.

[8] E. Mostaed, M. Sikora-Jasinska, A. Mostaed, S. Loffredo, A.G. Demir, B. Previtali, D. Mantovani, R. Beanland, M. Vedani, Novel Zn-based alloys for biodegradable stent applications: design, development and in vitro degradation, J. Mech. Behav. Biomed. Mater. 60 (2016) 581–602.

[9] C.F. Mills, Zinc in Human Biology, Springer London, 2013.

[10] N.R. Calhoun, J.C. Smith Jr., K.L. Becker, The role of zinc in bone metabolism, Clin. Orthop. Relat. Res. 103 (1974).

[11] M. Yamaguchi, H. Oishi, Y. Suketa, Stimulatory effect of zinc on bone formation in tissue culture, Biochem. Pharmacol. 36 (22) (1987) 4007–4012.

[12] M. Hambidge, Human zinc deficiency, J. Nutr. 130 (5) (2000) 1344S–1349S.

[13] H.N. Hoffman, R.L. Phyliky, C.R. Fleming, Zinc-induced copper deficiency, Gastroenterology 94 (2) (1988) 508–512.

[14] V. Hybasek, J. Kubasek, J. Capek, D. Alferi, J. Pinc, J. Jiru, J. Fojt, Influence of model environment complexity on corrosion mechanism of biodegradable zinc alloys, Corrosion Sci. 187 (2021), 109520.

[15] X. Liu, J. Sun, K. Qiu, Y. Yang, Z. Pu, L. Li, Y. Zheng, Effects of alloying elements (Ca and Sr) on microstructure, mechanical property and in vitro corrosion behavior of biodegradable Zn–1.5Mg alloy, J. Alloys Compd. 664 (2016) 444–452.

[16] A. Kafri, S. Ovadia, J. Goldman, J. Drelich, E. Aghion, The suitability of Zn–1.3%Fe alloy as a biodegradable implant, Material, Metals 8 (3) (2018) 153.

[17] K.D. Ralston, N. Birbilis, Effect of grain size on corrosion: a review, Corrosion 66 (7) (2010), 075005-075005-13.

[18] D. Zhu, I. Cockerill, Y. Su, Z. Zhang, J. Fu, K.-W. Lee, J. Ma, C. Okpokwasili, L. Tang, Y. Zheng, Y.-X. Qin, Y. Wang, Mechanical strength, biodegradation, and in vitro and in vivo biocompatibility of Zn biomaterials, ACS Appl. Mater. Interfaces 11 (7) (2019) 6809–6819.

[19] P.K. Bowen, J. Drelich, J. Goldman, Zinc exhibits ideal physiological corrosion behavior for bioabsorbable stents, Adv. Mater. 25 (18) (2013) 2577–2582.

[20] G. Li, H. Yang, Y. Zheng, X.-H. Chen, J.-A. Yang, D. Zhu, L. Ruan, K. Takashima, Challenges in the use of zinc and its alloys as biodegradable metals: perspective from biomechanical compatibility, Acta Biomater. 97 (2019) 23–45.

[21] H. Li, H. Yang, Y. Zheng, F. Zhou, K. Qiu, X. Wang, Design and characterizations of novel biodegradable ternary Zn-based alloys with IIA nutrient alloying elements Mg, Ca and Sr, Mater. Des. 83 (2015) 95–102.

[22] J. Čapek, J. Kubásek, J. Pinc, J. Drahokoupil, M. Čavojský, D. Vojtěch, Extrusion of the biodegradable ZnMg0.8Ca0.2 alloy – the influence of extrusion parameters on microstructure and mechanical characteristics, J. Mech. Behav. Biomed. Mater. 108 (2020), 103796.

[23] S. Sun, Y. Ren, L. Wang, B. Yang, H. Li, G. Qin, Abnormal effect of Mn addition on the mechanical properties of as-extruded Zn alloys, Mater. Sci. Eng., A 701 (2017) 129–133.

[24] X. Liu, J. Sun, Y. Yang, F. Zhou, Z. Pu, L. Li, Y. Zheng, Microstructure, mechanical properties, in vitro degradation behavior and hemocompatibility of novel Zn–Mg–Sr alloys as biodegradable metals, Mater. Lett. 162 (2016) 242–245.

[25] H. Yang, B. Jia, Z. Zhang, X. Qu, G. Li, W. Lin, D. Zhu, K. Dai, Y. Zheng, Alloying design of biodegradable zinc as promising bone implants for load-bearing applications, Nat. Commun. 11 (1) (2020) 401.

[26] C. Yao, Z. Wang, S.L. Tay, T. Zhu, W. Gao, Effects of Mg on microstructure and corrosion properties of Zn–Mg alloy, J. Alloys Compd. 602 (2014) 101–107.

[27] B. Jia, H. Yang, Z. Zhang, X. Qu, X. Jia, Q. Wu, Y. Han, Y. Zheng, K. Dai, Biodegradable Zn–Sr alloy for bone regeneration in rat femoral condyle defect model: in vitro and in vivo studies, Bioact. Mater. 6 (6) (2021) 1588–1604.

[28] S. Zhao, J.-M. Seitz, R. Eifler, H.J. Maier, R.J. Guillory, E.J. Earley, A. Drelich, J. Goldman, J.W. Drelich, Zn–Li alloy after extrusion and drawing: Structural, mechanical characterization, and biodegradation in abdominal aorta of rat, Mater. Sci. Eng. C 76 (2017) 301–312.

[29] B. Jia, H. Yang, Y. Han, Z. Zhang, X. Qu, Y. Zhuang, Q. Wu, Y. Zheng, K. Dai, In vitro and in vivo studies of Zn-Mn biodegradable metals designed for orthopedic applications, Acta Biomater. 108 (2020) 358–372.

[30] Y. Xie, L. Zhao, Z. Zhang, X. Wang, R. Wang, C. Cui, Fabrication and properties of porous Zn-Ag alloy scaffolds as biodegradable materials, Mater. Chem. Phys. 219 (2018) 433–443.

[31] X. Tong, D. Zhang, X. Zhang, Y. Su, Z. Shi, K. Wang, J. Lin, Y. Li, J. Lin, C. Wen, Microstructure, mechanical properties, biocompatibility, and in vitro corrosion and degradation behavior of a new Zn–5Ge alloy for biodegradable implant materials, Acta Biomater. 82 (2018) 197–204.

[32] H.F. Li, X.H. Xie, Y.F. Zheng, Y. Cong, F.Y. Zhou, K.J. Qiu, X. Wang, S.H. Chen, L. Huang, L. Tian, L. Qin, Development of biodegradable Zn-1X binary alloys with nutrient alloying elements Mg, Ca and Sr, Sci. Rep. 5 (1) (2015), 10719.

[33] W. Bednarczyk, J. Kawałko, M. Wątroba, N. Gao, M.J. Starink, P. Bała, T. G. Langdon, Microstructure and mechanical properties of a Zn-0.5Cu alloy processed by high-pressure torsion, Mater. Sci. Eng., A 776 (2020), 139047.

[34] J. Pinc, A. Školáková, P. Veřtát, J. Duchoň, J. Kubásek, P. Lejček, D. Vojtěch, J. Čapek, Microstructure evolution and mechanical performance of ternary Zn-0.8Mg-0.2Sr (wt. %) alloy processed by equal-channel angular pressing, Mater. Sci. Eng., A 824 (2021), 141809.

[35] W. Bednarczyk, M. Wątroba, J. Kawałko, P. Bała, Can zinc alloys be strengthened by grain refinement? A critical evaluation of the processing of low-alloyed binary zinc alloys using ECAP, Mater. Sci. Eng., A 748 (2019) 357–366.

[36] H. Gong, K. Wang, R. Strich, J.G. Zhou, In vitro biodegradation behavior, mechanical properties, and cytotoxicity of biodegradable Zn–Mg alloy, J. Biomed. Mater. Res. B Appl. Biomater. 103 (8) (2015) 1632–1640.

[37] J. Kubásek, J. Pinc, K. Hosová, K. Stráská, O. Molnárová, J. Duchoň, D. Nečas, M. Čavojský, M. Knapek, M. Godec, I. Paulin, D. Vojtěch, J. Čapek, The evolution of microstructure and mechanical properties of Zn-0.8Mg-0.2Sr alloy prepared by casting and extrusion, J. Alloys Compd. 906 (2022), 164308.

[38] D. Vojtěch, J. Kubásek, J. Šerák, P. Novák, Mechanical and corrosion properties of newly developed biodegradable Zn-based alloys for bone fixation, Acta Biomater. 7 (9) (2011) 3515–3522.

[39] H. Yang, X. Qu, W. Lin, D. Chen, D. Zhu, K. Dai, Y. Zheng, Enhanced osseointegration of Zn-Mg composites by tuning the release of Zn ions with sacrificial Mg-rich anode design, ACS Biomater. Sci. Eng. 5 (2) (2019) 453–467.

[40] L. Ye, H. Huang, C. Sun, X. Zhuo, Q. Dong, H. Liu, J. Ju, F. Xue, J. Bai, J. Jiang, Effect of grain size and volume fraction of eutectic structure on mechanical properties and corrosion behavior of as-cast Zn–Mg binary alloys, J. Mater. Res. Technol. 16 (2022) 1673–1685.

[41] X. Liu, H. Yang, P. Xiong, W. Li, H.-H. Huang, Y. Zheng, Comparative studies of Tris-HCl, HEPES and NaHCO3/CO2 buffer systems on the biodegradation behaviour of pure Zn in NaCl and SBF solutions, Corrosion Sci. 157 (2019) 205–219.

[42] L. Liu, Y. Meng, C. Dong, Y. Yan, A.A. Volinsky, L.-N. Wang, Initial formation of corrosion products on pure zinc in simulated body fluid, J. Mater. Sci. Technol. 34 (12) (2018) 2271–2282.

[43] D. Jain, S. Pareek, A. Agarwala, R. Shrivastava, W. Sassi, S.K. Parida, D. Behera, Effect of exposure time on corrosion behavior of zinc-alloy in simulated body fluid solution: electrochemical and surface investigation, J. Mater. Res. Technol. 10 (2021) 738–751.

[44] L. Müller, F.A. Müller, Preparation of SBF with different HCO3- content and its influence on the composition of biomimetic apatites, Acta Biomater. 2 (2) (2006) 181–189.

[45] V. Wagener, S. Virtanen, Influence of electrolyte composition (simulated body fluid vs. Dulbecco's modified eagle's medium), temperature, and solution flow on the biocorrosion behavior of commercially pure Mg, Corrosion 73 (12) (2017) 1413–1422.

[46] S. Ban, S. Maruno, Effect of temperature on electrochemical deposition of calcium phosphate coatings in a simulated body fluid, Biomaterials 16 (13) (1995) 977–981.

[47] K. Thompson, D. Lawrence, D.J. Larson, J.D. Olson, T.F. Kelly, B. Gorman, In situ site-specific specimen preparation for atom probe tomography, Ultramicroscopy 107 (2) (2007) 131–139.

[48] S. Sadewasser, T. Glatzel, Kelvin Probe Force Microscopy: from Single Charge Detection to Device Characterization, Springer International Publishing, 2018.

[49] D. Nečas, P. Klapetek, Gwyddion: an open-source software for SPM data analysis, Cent. Eur. J. Phys. 10 (1) (2012) 181–188.

[50] M. Klinger, More features, more tools, more CrysTBox, J. Appl. Crystallogr. 50 (4) (2017) 1226–1234.

[51] S. Gates-Rector, T. Blanton, The Powder Diffraction File: a quality materials characterization database, Powder Diffr. 34 (4) (2019) 352–360.

[52] M.C. Kuo, S.K. Yen, The process of electrochemical deposited hydroxyapatite coatings on biomedical titanium at room temperature, Mater. Sci. Eng. C 20 (1) (2002) 153–160.

[53] I. Suzuki, The behavior of corrosion products on zinc in sodium chloride solution, Corrosion Sci. 25 (11) (1985) 1029–1034.

[54] G.J. Brug, A.L.G. van den Eeden, M. Sluyters-Rehbach, J.H. Sluyters, The analysis of electrode impedances complicated by the presence of a constant phase element, J. Electroanal. Chem. Interfacial Electrochem. 176 (1) (1984) 275–295.

[55] Y. Meng, L. Liu, D. Zhang, C. Dong, Y. Yan, A.A. Volinsky, L.-N. Wang, Initial formation of corrosion products on pure zinc in saline solution, Bioact. Mater. 4 (2019) 87–96.

[56] D.A. Wollman, D.E. Newbury, G.C. Hilton, K.D. Irwin, D.A. Rudman, L.L. Dulcie, N. F. Bergren, J.M. Martinis, Microcalorimeter energy dispersive spectrometry for low voltage SEM, Microsc. Microanal. 5 (S2) (1999) 304–305.

[57] J. Pinc, J. Čapek, J. Kubásek, F. Průša, V. Hybášek, P. Veřtát, I. Sedlářová, D. Vojtěch, Characterization of a Zn-Ca5(PO4)3(OH) composite with a high content of the hydroxyapatite particles prepared by the spark plasma sintering process, Metals 10 (3) (2020) 372.

[58] X. Shao, X. Wang, F. Xu, T. Dai, J.G. Zhou, J. Liu, K. Song, L. Tian, B. Liu, Y. Liu, In vivo biocompatibility and degradability of a Zn–Mg–Fe alloy osteosynthesis system, Bioact. Mater. 7 (2022) 154–166.

[59] J. Čapek, J. Pinc, Š. Msallamová, E. Jablonská, P. Veřtát, J. Kubásek, D. Vojtěch, Thermal plasma spraying as a new approach for preparation of zinc biodegradable scaffolds: a complex material characterization, J. Therm. Spray Technol. 28 (4) (2019) 826–841.

[60] T.B. Massalski, H. Okamoto, P. Subramanian, L. Kacprzak, W.W. Scott, Binary Alloy Phase Diagrams, American society for metals Metals Park, OH, 1986.

[61] J. Čapek, J. Kubásek, J. Pinc, J. Maňák, O. Molnárová, A. Drahokoupil, M. Čavojský, ZnMg0.8Ca0.2 (wt%) biodegradable alloy – the influence of thermal treatment and extrusion on microstructural and mechanical characteristics, Mater. Char. 162 (2020), 110230.

[62] Z. Tang, J. Niu, H. Huang, H. Zhang, J. Pei, J. Ou, G. Yuan, Potential biodegradable Zn-Cu binary alloys developed for cardiovascular implant applications, J. Mech. Behav. Biomed. Mater. 72 (2017) 182–191.

[63] T. Prosek, D. Persson, J. Stoulil, D. Thierry, Composition of corrosion products formed on Zn–Mg, Zn–Al and Zn–Al–Mg coatings in model atmospheric conditions, Corrosion Sci. 86 (2014) 231–238.

[64] K.D. Ralston, N. Birbilis, C.H.J. Davies, Revealing the relationship between grain size and corrosion rate of metals, Scripta Mater. 63 (12) (2010) 1201–1204.

[65] P. Lejček, Grain boundaries: description, structure and thermodynamics, in: P. Lejček (Ed.), Grain Boundary Segregation in Metals, Springer Berlin Heidelberg, Berlin, Heidelberg, 2010, pp. 5–24.

[66] P. Volovitch, C. Allely, K. Ogle, Understanding corrosion via corrosion product characterization: I. Case study of the role of Mg alloying in Zn–Mg coating on steel, Corrosion Sci. 51 (6) (2009) 1251–1262.

[67] X. Liu, J. Sun, F. Zhou, Y. Yang, R. Chang, K. Qiu, Z. Pu, L. Li, Y. Zheng, Micro-alloying with Mn in Zn–Mg alloy for future biodegradable metals application, Mater. Des. 94 (2016) 95–104.

[68] O. Knacke, O. Kubaschewski, K. Hesselmann, Thermochemical Properties of Inorganic Substances II, Springer, 1991.

[69] O. Knacke, O. Kubaschewski, K. Hesselmann, Thermochemical Properties of Inorganic Substances, Springer-Verlag, 1991.

[70] I. Barin, F. Sauert, E. Schultze-Rhonhof, W.S. Sheng, Thermochemical Data of Pure Substances: La-Zr, 1993. VCH.

[71] M. Morishita, K. Koyama, Calorimetric study of MgZn2 and Mg2Zn11, Int. J. Mater. Res. 94 (9) (2003) 967–971.

[72] R. Xin, Y. Luo, A. Zuo, J. Gao, Q. Liu, Texture effect on corrosion behavior of AZ31 Mg alloy in simulated physiological environment, Mater. Lett. 72 (2012) 1–4.

[73] A.K. Vasudevan, K. Sadananda, Role of internal stresses on the incubation times during stress corrosion cracking, Metall. Mater. Trans. 42 (2) (2011) 396–404.

[74] K. Törne, M. Larsson, A. Norlin, J. Weissenrieder, Degradation of zinc in saline solutions, plasma, and whole blood, J. Biomed. Mater. Res. B Appl. Biomater. 104 (6) (2016) 1141–1151.

[75] M.M. Alves, T. Prošek, C.F. Santos, M.F. Montemor, Evolution of the in vitro degradation of Zn–Mg alloys under simulated physiological conditions, RSC Adv. 7 (45) (2017) 28224–28233.

[76] K. Klíma, D. Ulmann, M. Bartoš, M. Španko, J. Dušková, R. Vrbová, J. Pinc, J. Kubásek, M. Vlk, T. Ulmannová, R. Foltán, E. Brizman, M. Drahoš, M. Beňo, V. Machoň, J. Čapek, A complex evaluation of the in-vivo biocompatibility and degradation of an extruded ZnMgSr absorbable alloy implanted into rabbit bones for 360 days, Int. J. Mol. Sci. 22 (24) (2021), 13444.

[77] K. Klíma, D. Ulmann, M. Bartoš, M. Španko, J. Dušková, R. Vrbová, J. Pinc, J. Kubásek, T. Ulmannová, R. Foltán, E. Brizman, M. Drahoš, M. Beňo, J. Čapek, Zn–0.8Mg–0.2Sr (wt.%) absorbable screws—an in-vivo biocompatibility and degradation pilot study on a rabbit model, Materials 14 (12) (2021) 3271.

[78] S.-J. Malgorzata, M. Ehsan, G. Jeremy, D.J. W, Albumins inhibit the corrosion of absorbable Zn alloys at initial stages of degradation, Surf. Innov. 8 (4) (2020) 234–249.

[79] M. Wang, L. Yang, X. Zhu, L. Yang, Z. Song, Influence of enzymes on the in vitro degradation behavior of pure Zn in simulated gastric and intestinal fluids, ACS Omega 8 (1) (2023) 1331–1342.

[80] H. Haase, S. Hebel, G. Engelhardt, L. Rink, The biochemical effects of extracellular Zn2+ and other metal ions are severely affected by their speciation in cell culture media, Metallomics 7 (1) (2014) 102–111.

[81] P. Li, Absorbable Zinc-Based Alloy for Craniomaxillofacial Osteosynthesis Implants, Universität Tübingen, 2020.

[82] J. Ma, N. Zhao, D. Zhu, Bioabsorbable zinc ion induced biphasic cellular responses in vascular smooth muscle cells, Sci. Rep. 6 (1) (2016), 26661.

[83] P.B. Moser-Veillon, Zinc: consumption patterns and dietary recommendations, J. Am. Diet Assoc. 90 (1990) 1089+.

[84] J.C.T. Farge, Recrystallization of Zinc Alloys, McGill University (Canada), 1965.

[85] F. Menan, G. Henaff, Influence of frequency and exposure to a saline solution on the corrosion fatigue crack growth behavior of the aluminum alloy 2024, Int. J. Fatig. 31 (11) (2009) 1684–1695.

[86] T. Demir, M. Özkaya, Mechanical testing standards of orthopedic implants, in: F. Korkusuz (Ed.), Musculoskeletal Research and Basic Science, Springer International Publishing, Cham, 2016, pp. 61–91.